https://doi.org/10.5194/egusphere-2026-940
Preprint. Discussion started: 13 March 2026

What is the neutral wind in height-integrated ionospheric electrodynamics?

Spencer Mark Hatch[1], Johnathan K. Burchill[2], Heikki Vanhamäki[3], Rafael Luiz Araujo de Mesquita[4], and Karl Magnus Laundal[5]

[1]Department of Physics and Technology, University of Bergen, Bergen, Norway
[2]Department of Physics and Astronomy, University of Calgary, Calgary, Alberta, Canada
[3]Space Physics and Astronomy Research Unit, University of Oulu, Oulu, Finland
[4]Johns Hopkins University Applied Physics Laboratory, Laurel, MD, USA
[5]Division of Geomagnetism and Geospace, DTU Space, Technical University of Denmark, Kongens Lyngby, Denmark

Correspondence: Spencer Mark Hatch (spencer.hatch@uib.no)

Abstract.

In many studies of the electrodynamics of the coupled ionosphere-thermosphere (IT) system at high latitudes, the ionosphere is represented as a two-dimensional spherical shell and the height-integrated ionospheric Ohm's law is used to understand IT electrodynamic coupling. Thermospheric winds play a central role in IT electrodynamics, but they are generally ignored in existing empirical models and assimilative methods. While the primary issue is a lack of comprehensive wind measurements, there is also a gap in the literature on how to represent the thermospheric winds—which often exhibit strong variations with altitude—in a height-integrated description of high-latitude IT electrodynamics, and what the associated sources of error might be. Here we highlight that there is in general no single suitable definition of the neutral wind term in high-latitude, height-integrated IT electrodynamics. Instead, two neutral wind terms weighted by Hall and Pedersen conductivities appear in the height-integrated Ohm's law. Using altitude profiles of neutral winds and ionospheric conductivities respectively derived from sounding rocket chemical release experiments near Poker Flat, Alaska, and Poker Flat Incoherent Scatter Radar (PFISR) measurements, we find magnitude differences of order 10–100 m/s between the two neutral wind terms. The difference in magnitude increases with increasing geomagnetic activity. We show that a commonly used expression for Joule heating in terms of height-integrated quantities is a lower bound of the actual height-integrated Joule heating. We find experimentally that the relative error associated with the term that depends exclusively on the winds decreases with increasing geomagnetic activity. We also show that the thermospheric winds at the altitude at which the Pedersen conductivity peaks is the best proxy for the thermospheric wind term in height-integrated, high-latitude electrodynamics.

1 Introduction

Earth's overlapping ionosphere-thermosphere (IT) region is the site of mechanical and electrodynamic coupling between the neutral atmosphere and plasmas of both terrestrial (magnetospheric and ionospheric) and extraterrestrial (solar wind) origin.

https://doi.org/10.5194/egusphere-2026-940
Preprint. Discussion started: 13 March 2026

Much of the electrodynamics within this region can be described in terms of a three-fluid model consisting of neutral, ion, and electron fluids in the presence of a strong background magnetic field (see Section 9.5 in Parker, 2007).

A common point of reference for a vast number of experimental investigations of high-latitude IT electrodynamics is the component of the ionospheric Ohm's law that is perpendicular to the main magnetic field, assuming steady-state stress balance between Lorentz and collisional drag forces and neglecting all other forces in the ion momentum equation (Section 5 in Chapman, 1956; Section 3.2.1 in Vasyliunas, 2012):

$$\mathbf{j}_\perp = \sigma_P \left(\mathbf{E}_\perp + \mathbf{u} \times \mathbf{B}\right) + \sigma_H \mathbf{b} \times \left(\mathbf{E}_\perp + \mathbf{u} \times \mathbf{B}\right), \tag{1}$$

with $\mathbf{j}_\perp$ the perpendicular current density, σ_P and σ_H the Pedersen and Hall conductivities, and $\mathbf{E}_\perp$, $\mathbf{B}$, and $\mathbf{u}$ the perpendicular ionospheric electric field, the total (background plus perturbation) magnetic field, and the thermospheric wind. The corresponding Joule heating (heating rate per volume) is given by

$$w_J = \mathbf{j}_\perp \cdot \left(\mathbf{E}_\perp + \mathbf{u} \times \mathbf{B}\right) = \sigma_P \left| \left(\mathbf{E}_\perp + \mathbf{u} \times \mathbf{B}\right) \right|^2. \tag{2}$$

Both $\mathbf{j}_\perp$ and w_J are independent of reference frame in (magnetic) Galilean relativity (Mannucci et al., 2022) by virtue of the fact that they are defined in terms of the sum of the electric field and the "neutral wind dynamo" $\mathbf{u} \times \mathbf{B}$.

Some notable experimental investigations of Equations 1 and 2 include that of Thayer (1998) and those based on the Joule II suborbital sounding rocket campaign (Sangalli et al., 2009; Burchill et al., 2012). The former used incoherent scatter radar measurements at a temporal resolution of ∼17 min to present the first examination of how the neutral wind $\mathbf{u}$ modifies height profiles of Joule heating. The Joule II-based study of Sangalli et al. (2009) used in situ measurements of electric field, bulk ion drift, neutral wind, and electron density in the vicinity of a relatively quiescent auroral breakup in northern Alaska to estimate the errors in *E*-region ion-neutral momentum transfer collision frequency and Joule heating altitude profiles that would arise if the neutral winds were assumed to be zero. In their separate analysis of these and additional rocket and ground-based observations from the same campaign, Burchill et al. (2012) found evidence for horizontal or vertical structuring in ion-neutral collision frequencies on scales of 1–10 km.

Comprehensive measurements of altitude profiles such as those presented by Sangalli et al. (2009) and Burchill et al. (2012) are rare. Much more frequently one encounters a height-integrated form of the ionospheric Ohm's law:

$$\mathbf{J}_\perp = \Sigma_P \left(\mathbf{E}_\perp + \mathbf{U} \times \mathbf{B}\right) + \Sigma_H \mathbf{b} \times \left(\mathbf{E}_\perp + \mathbf{U} \times \mathbf{B}\right), \tag{3}$$

where Σ_P and Σ_H are the Pedersen and Hall conductances (conductivities integrated over altitude, explicitly $\Sigma_c = \int \sigma_c dh$ with c either H or P). This form is obtained by integrating Equation 3 over altitude assuming that $\mathbf{B}$ is radial, that $\mathbf{B}$ and $\mathbf{E}_\perp$ are independent of altitude over ionospheric *E*- and *F*-region altitudes (∼100–250 km), and that $\mathbf{U}$ is the height-averaged neutral wind or a "representative" or "effective" neutral wind, which is typically left undefined and most often simply taken to be zero in Earth's rotating frame of reference. (Appendix A provides a brief summary of the implications of assuming the E-field is constant with altitude.) One also encounters an expression for height-integrated Joule heating rate,

$$W_J = \int w_J \, dh = \mathbf{J}_\perp \cdot \left(\mathbf{E}_\perp + \mathbf{U} \times \mathbf{B}\right) = \Sigma_P \left(\mathbf{E}_\perp + \mathbf{U} \times \mathbf{B}\right)^2, \tag{4}$$

https://doi.org/10.5194/egusphere-2026-940
Preprint. Discussion started: 13 March 2026

that is also defined in terms of a typically unspecified or unused effective neutral wind $\mathbf{U}$. Last, one encounters estimates of ionospheric conductances via the expressions likewise defined in terms of $\mathbf{U}$,

$$\Sigma_H = \pm\hat{\mathbf{r}} \cdot [\mathbf{J}_\perp \times (\mathbf{E}_\perp + \mathbf{U} \times \mathbf{B})] / |\mathbf{E}_\perp + \mathbf{U} \times \mathbf{B}|^2; \quad (5)$$

$$\Sigma_P = \mathbf{J}_\perp \cdot (\mathbf{E}_\perp + \mathbf{U} \times \mathbf{B}) / |\mathbf{E}_\perp + \mathbf{U} \times \mathbf{B}|^2; \quad (6)$$

where the upper and lower signs of the RHS in Equation 5 are respectively for the Northern and Southern Hemisphere.

The approach represented by Equation 4 for estimating height-integrated Joule heating based on height-integrated quantities dates at least back to the work of Cole (1975) and continues to be used widely (see Thayer, 1998, and references therein). The study of Billett et al. (2018) stands out as the only observational study of global distributions of ionospheric Joule heating that has included information, via an empirical model, about an effective wind pattern. On the other hand, the approach represented by Equations 5–6 for estimating conductances based on height-integrated quantities originates with Amm (2001). This approach has been used by a number of studies over the past two decades, and has elsewhere been referred to as the "electrodynamic method" (e.g., Green et al., 2007; Weimer and Edwards, 2021; Hatch et al., 2024). To our knowledge, all published studies in which conductance distributions have been estimated experimentally via Equations 5–6 have assumed $\mathbf{U} = 0$.

The height-integrated approach to ionospheric electrodynamics represented by Equations 3–6 is heavily simplified: Earth's magnetic field lines are not radial, ionospheric electric fields do not necessarily map along field lines (Farley, 1959), and the horizontal components of the neutral wind exhibit the nearly permanent presence of vertical shears over altitudes of 80 to 140 km (Heppner and Miller, 1982; Larsen, 2002; Sangalli et al., 2009). More advanced treatments of ionospheric electrodynamics that account for such complications, such as that presented by Richmond (1995), nevertheless remain unused in a large number of experimental studies and data assimilation techniques (e.g., Richmond and Kamide, 1988; Matsuo, 2020; Laundal et al., 2022, 2025a), primarily for lack of a body of robust 3D measurements of the IT system needed to make use of them (Palmroth et al., 2021). For similar reasons, in the majority of existing global MHD models the coupling between the magnetosphere and the IT system is founded on what Mannucci et al. (2022) term a "key magnetosphere-ionosphere coupling equation" derived from current continuity (their Equation 11; see also Merkin and Lyon, 2010; Mukhopadhyay et al., 2021, and references therein) in which the neutral wind is assumed to be zero or constant with altitude.

In this study, we explore some of the implications of the commonly employed assumption that the neutral wind is independent of altitude that is necessary to arrive at Equations 3–6 as well as the current continuity equation used in magnetosphere-ionosphere coupling. In Section 2 we summarize central quantities and equations in a height-integrated description of IT electrodynamics when the neutral wind is not assumed to be independent of altitude. In Section 3 we present three basic questions that are raised by this alternative formalism, and answer them using neutral wind profiles derived from rocket-borne trimethylaluminum (TMA) chemical release experiments launched from the Poker Flat Research Range (PFRR) between 2007 and 2018 together with conductivity profiles calculated from measurements made by the Poker Flat Incoherent Scatter Radar (PFISR). In Section 4 we summarize our findings, and discuss how they can be used to understand the role of the neutral winds in 2D descriptions of IT electrodynamics.

https://doi.org/10.5194/egusphere-2026-940
Preprint. Discussion started: 13 March 2026

2 Defining the neutral wind in height-integrated IT electrodynamics

If one assumes that $\mathbf{u}$ *does* vary with height, integration of Ohm's law (Equation 1) over ionospheric altitudes yields

$$\mathbf{J}_\perp = \Sigma_P \mathbf{F}_P + \Sigma_H \hat{\mathbf{b}} \times \mathbf{F}_H \tag{7}$$

where

$$\mathbf{F}_c = \mathbf{E}_\perp + \mathbf{U}_c \times \mathbf{B}; \tag{8}$$

$$\mathbf{U}_c = \frac{1}{\Sigma_c} \int \sigma_c \, \mathbf{u} \, dh; \tag{9}$$

and c is either H or P. The integration is performed over all ionospheric altitudes. We refer to the conductivity-weighted neutral wind terms $\mathbf{U}_H$ and $\mathbf{U}_P$ as the Hall-weighted or Pedersen-weighted neutral winds. The latter has been termed the "effective neutral wind" by Lu et al. (1995) and plays a role in estimates of height-integrated Joule heating and the Pedersen conductance, which we discuss later in this section. The distinction between the Hall-weighted and Pedersen-weighted neutral winds disappears when the two conductivity profiles differ by no more than a constant factor, or when the neutral wind $\mathbf{u}$ does not vary with altitude. As noted in the Introduction, these idealized conditions are virtually never manifest in measured altitude profiles of the conductivities and neutral winds.

Integrating the right-hand side of the expression for Joule heating density (2), we obtain the height-integrated Joule heating rate

$$W_J = \int w_J \, dh = \int \sigma_P |\left(\mathbf{E}_\perp + \mathbf{u} \times \mathbf{B}\right)|^2 \, dh = \Sigma_P \left[E_\perp^2 + 2\mathbf{E}_\perp \cdot \left(\mathbf{U}_P \times \mathbf{B}\right)\right] + \int \sigma_P \|\mathbf{u} \times \mathbf{B}\|^2 \, dh. \tag{10}$$

Because of the integral in the last term involving $|\mathbf{u} \times \mathbf{B}|^2$, this expression cannot directly be brought into the more familiar form $\Sigma_P \left(\mathbf{E}_\perp + \mathbf{U} \times \mathbf{B}\right)^2$ for some appropriately chosen $\mathbf{U}$ (cf. Equation 4). However, one may show explicitly via the Cauchy-Bunyakovsky-Schwarz inequality (see Appendix B) that $\int \sigma_P \|\mathbf{u} \times \mathbf{B}\|^2 \, dh \geq \Sigma_P \left(\mathbf{U}_P \times \mathbf{B}\right)^2$. Then the following inequalities hold:

$$\begin{aligned} &W_J \geq \Sigma_P \left(\mathbf{E}_\perp + \mathbf{U}_P \times \mathbf{B}\right)^2 = \Sigma_P F_P^2; \\ &\Sigma_P \leq W_J / F_P^2. \end{aligned} \tag{11}$$

Thus when the "effective" neutral wind $\mathbf{U}$ is specified to be the Pedersen-weighted neutral wind $\mathbf{U}_P$ in Equations 4 and 6, these equations are in fact lower and upper bounds, respectively, on the true height-integrated Joule heating and Pedersen conductance. When the neutral wind does not vary with altitude we have $\mathbf{U}_P = \mathbf{U}_H = \mathbf{U}$ in Inequality 11, such that the height-integrated Joule heating $W_J = \Sigma_P (\mathbf{E} + \mathbf{U} \times \mathbf{B})^2$ and the Pedersen conductance $\Sigma_P = W_J / (\mathbf{E} + \mathbf{U} \times \mathbf{B})^2$ as given by Equations 4 and 6.

From the foregoing we see that for estimation of height-integrated Joule heating, the Pedersen-weighted neutral wind $\mathbf{U}_P$ constitutes the most natural definition of the "effective" neutral wind, as indirectly suggested by Lu et al. (1995).

https://doi.org/10.5194/egusphere-2026-940
Preprint. Discussion started: 13 March 2026

3 Experimental investigation of Hall- and Pedersen-weighted neutral winds

Equations 7–9 illustrate that there is in general not one, but two, neutral wind terms in height-integrated treatments of IT electrodynamics. The neutral wind appears as two separate terms weighted separately by the Hall and Pedersen conductivity profiles, here defined by Equation 9 and respectively denoted by $\mathbf{U}_H$ and $\mathbf{U}_P$. This situation raises the following questions:

1. How large is the observed difference between $\mathbf{U}_H$ and $\mathbf{U}_P$? (Section 3.2)
2. How much better are various rule-of-thumb approximations for the neutral wind (e.g., the suggestion from Lu et al., 1995, that the "winds at 160 km" are representative of the "effective neutral wind") than simply assuming $\mathbf{U}_H = \mathbf{U}_P = \mathbf{u} = 0$? (Section 3.3)
3. How much does the lower-bound approximation $\Sigma_P(\mathbf{U}_P \times \mathbf{B})^2$ underestimate the true contribution of the purely wind-dependent term $\int \sigma_P \|\mathbf{u} \times \mathbf{B}\|^2 dh$ in the expression for height-integrated Joule heating given by Equation 10? (Section 3.4)

To answer these questions we use horizontal neutral wind profiles derived from TMA chemical release experiments carried by sounding rockets during five campaigns launched from PFRR (Mesquita, 2021, and references therein), as well as vertical conductivity profiles derived from PFISR measurements and empirical models of ionospheric and atmospheric composition, atmospheric temperature, and Earth's magnetic field.

3.1 Measurements and models

Figure 1 shows a summary of the 15 wind profiles used in this study, with the zonal and meridional components displayed respectively in the left and center columns, and the horizontal magnitudes in the right column. The vertical component is not estimated and is ignored throughout this study. The text label at right shows the date, campaign name, and Kp value for each group of wind profiles. The chronological ordering of the rows of Figure 1 coincidentally also orders the wind profiles by Kp, aside from the last row (Super Soaker campaign) for which Kp was lowest (Kp $= 0.3$). The magnitudes of the wind profiles show a clear tendency to increase with increasing Kp.

Table 1 summarizes some details of each rocket, including the time of each measurement (center time of images used for triangulation of chemical release experiments) and the availability of PFISR measurements.

For each wind profile shown in Figure 1 we calculate corresponding $\mathbf{U}_H$ and $\mathbf{U}_P$ vectors via Equation 9. This calculation requires conductivity profiles, which we calculate using PFISR measurements, the NRLMSIS®2.0 empirical atmospheric model (Emmert et al., 2020), and the International Reference Ionosphere (IRI) 2016 model (Bilitza et al., 2017), following the methodology of Ieda (2020). The steps of this process are summarized and illustrated in Appendix C and Figure C1.

3.2 Statistics of $\mathbf{U}_H$ and $\mathbf{U}_P$

After performing the procedure described in the previous subsection for all 15 neutral wind profiles, we obtain the estimates of $\mathbf{U}_H$ and $\mathbf{U}_P$ as well as their difference $(\mathbf{U}_H - \mathbf{U}_P)$ shown in Figure 2a. For these neutral wind profiles the zonal component of

https://doi.org/10.5194/egusphere-2026-940
Preprint. Discussion started: 13 March 2026

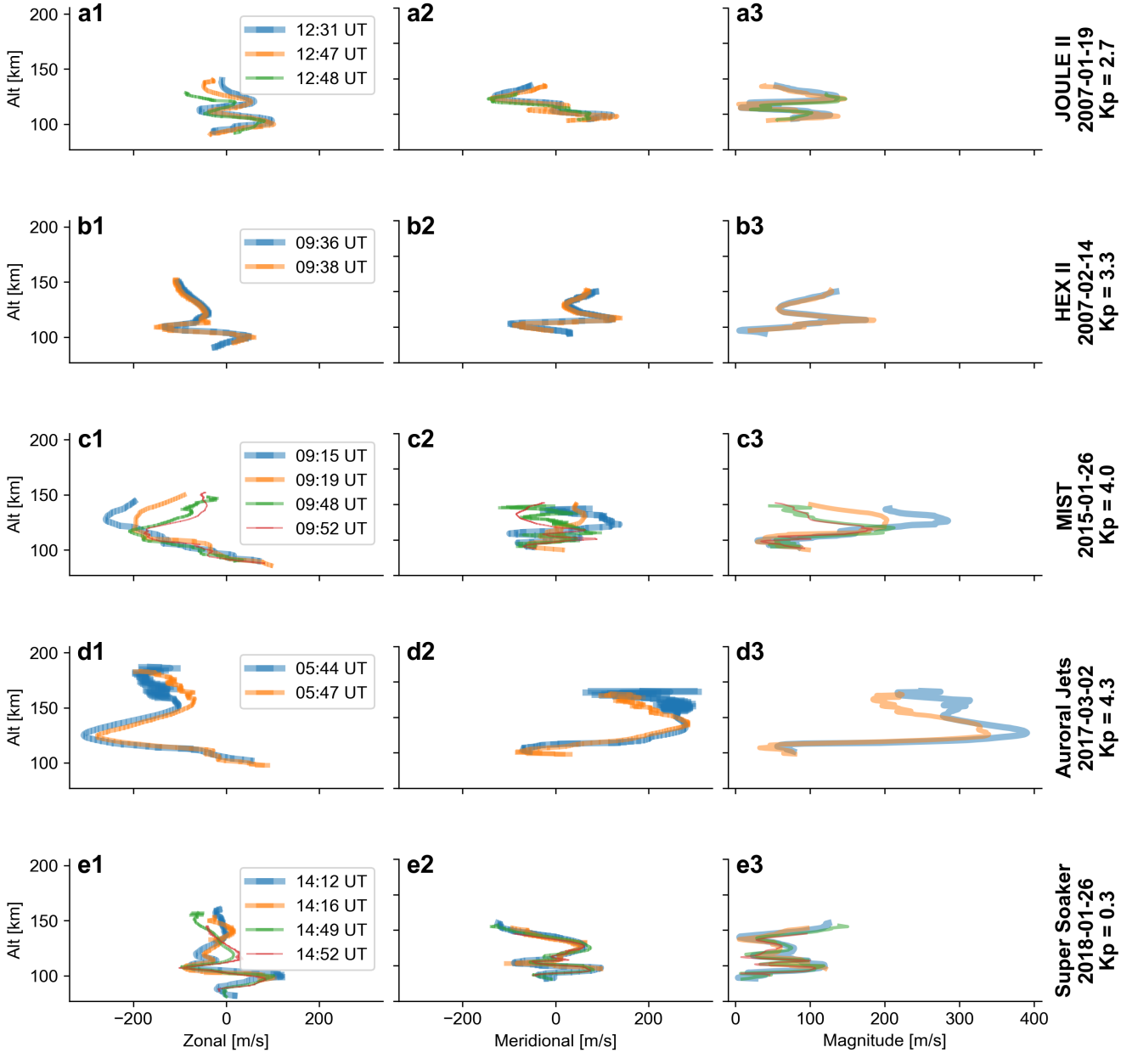

Figure 1. Summary of neutral wind profiles used in this study, given in the same order as the rocket campaigns in Table 1. The zonal and meridional components are shown in the left and center columns, with the magnitude profiles shown in the right column. The campaign name and degree of geomagnetic activity are indicated in the caption at far right in each row.

https://doi.org/10.5194/egusphere-2026-940
Preprint. Discussion started: 13 March 2026

Table 1. Rockets from which neutral wind measurements are used in this study.

Rocket	Date	Launch [UT]	Alt range [km]	PFISR alt range[a,b] [km]	PFISR meas. [UT]	Kp	Reference
Joule II	2007-01-19	12:31	93.5–140.0	91–300	12:30:00	2.7	Burchill et al. (2012)
		12:47	91–140	91–274	12:45:20		Sangalli et al. (2009)
		12:48	92–128.5	91–274	12:45:20		
HEX II	2007-02-14	09:36	91–150	91–326	09:46:08	3.3	Scott (2009)
		09:38	95–152	91–326	09:46:08		
MIST	2015-01-26	09:15	90–144		09:14:55	4.0	Larsen et al. (2022)
		09:19	86–150		09:19:56		
		09:48	90–148	83–345	09:44:55		
		09:52	88–152		09:49:56		
Auroral	2017-03-02	05:44	102–187		05:44:11	4.3	
Jets		05:47	98–183		05:47:15		Akbari et al. (2022)
Super	2018-01-26	14:12	82–320		14:03:36	0.3	Mesquita et al. (2020)
Soaker		14:16	96–153	88–320	14:18:41		
		14:49	81–157	85–347	14:48:51		
		14:52	86–145	85–347	14:48:51		

[a] We exclude PFISR measurements for which $\sigma_{n_e}/n_e \geq 1$. (n_e: plasma density. σ_{n_e}: plasma density uncertainty.)

[b] Valid PFISR measurements are available over 87–345 km unless otherwise noted. Vertical (elevation = 90°) beam measurements are used.

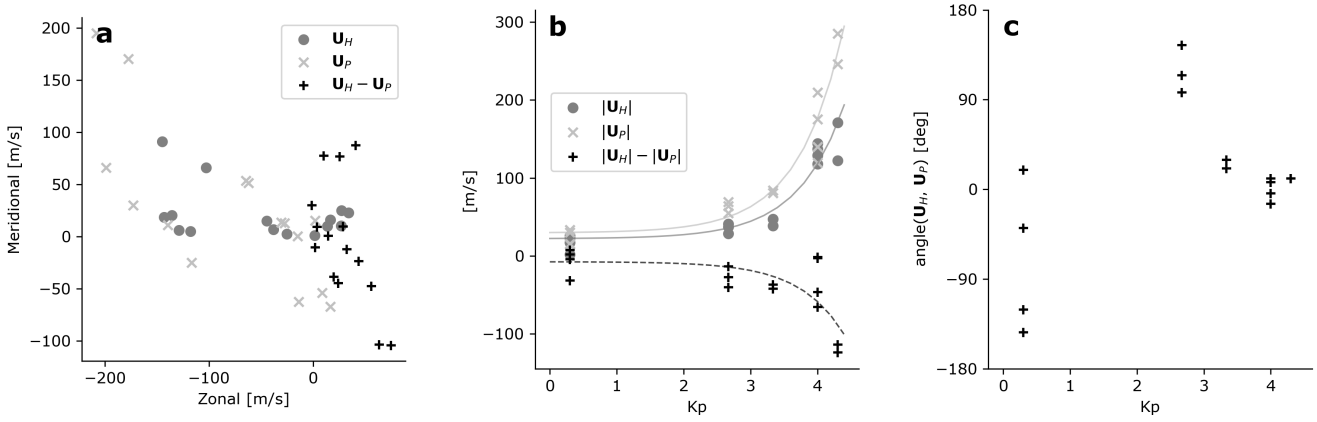

Figure 2. (a) Statistics of $\mathbf{U}_H$, $\mathbf{U}_P$, and $\mathbf{U}_H - \mathbf{U}_P$. (b) The magnitude of $\mathbf{U}_H$ and $\mathbf{U}_P$, and the difference in magnitudes, versus Kp. The solid lines are nonlinear fits of the form $a\exp(\mathrm{Kp}/b) + c$ to $|\mathbf{U}_H|$ and $|\mathbf{U}_P|$, and the dashed line their difference. (c) The angle measured from the direction of $\mathbf{U}_H$ to the direction $\mathbf{U}_P$ versus Kp. These plots answer Question 1 posed at the beginning of Section 3 ("How large is the observed difference between $\mathbf{U}_H$ and $\mathbf{U}_P$?").

https://doi.org/10.5194/egusphere-2026-940
Preprint. Discussion started: 13 March 2026

$\mathbf{U}_H$ and $\mathbf{U}_P$ tend to be negative (westward), while the meridional components tend to be positive (northward). The magnitudes of $\mathbf{U}_H$ and $\mathbf{U}_P$ are of order 10–100 m/s. Given the magnitude of the geomagnetic field at PFRR (∼54,000 nT at 110-km altitude), these magnitudes correspond to electric field equivalents of ∼0.5–5 mV/m.

Figure 2b plots the magnitudes of $\mathbf{U}_H$ and $\mathbf{U}_P$ and shows that they increase approximately exponentially with increasing K_p. The difference $|\mathbf{U}_H| - |\mathbf{U}_P|$ (black crosses) is almost everywhere negative; the only two instances in which $|\mathbf{U}_H| > |\mathbf{U}_P|$ are found for Kp $= 0.3$. The difference is increasingly negative for increasing Kp.

The solid lines in Figure 2 demonstrate that an exponential function of the form $a \exp(\mathrm{Kp}\,/\,b) + c$ suitably describes the magnitudes of $\mathbf{U}_H$ and $\mathbf{U}_P$. The dashed line displays the difference between these fit functions and follows the overall trend of $|\mathbf{U}_H| - |\mathbf{U}_P|$. Fit parameters for $|\mathbf{U}_H|$ and $|\mathbf{U}_P|$ are derived by performing a nonlinear regression that minimizes the residuals for all three sets of points shown in Figure 2 simultaneously, subject to Huber loss (Huber, 1973), to provide a robust estimate of the best-fit parameters. The fits are performed using the `least_squares` function of SciPy (Virtanen et al., 2020). We obtain similar results (not shown) with a standard linear loss function and when each of the sets of points are fit separately.

Figure 2c displays the angle between $\mathbf{U}_H$ and $\mathbf{U}_P$ measured from the direction of $\mathbf{U}_H$ to the direction of $\mathbf{U}_P$. This is calculated as

$$\mathrm{angle}(\mathbf{U}_H, \mathbf{U}_P) = \mathrm{atan2}\,(U_{H,y}, U_{H,x}) - \mathrm{atan2}\,(U_{P,y}, U_{P,x})\,,$$

where x and y refer respectively to the zonal and meridional wind components. The angle appears to tend toward zero for increasing Kp, indicating that $\mathbf{U}_H$ and $\mathbf{U}_P$ tend to become more aligned with increasing geomagnetic activity.

3.3 Proxies for the Hall- and Pedersen-weighted neutral winds

Here we address Question 2 posed at the beginning of this section: How much better are various rule-of-thumb approximations for the neutral wind than simply assuming $\mathbf{U}_H = \mathbf{U}_P = \mathbf{u} = 0$? To answer this question, Figure 3a shows the error distribution $\mathrm{Error}\,(\mathbf{U}_P = \mathbf{u}_{\mathrm{proxy}}) = |\mathbf{U}_P - \mathbf{u}_{\mathrm{proxy}}|$ associated with the assumption $\mathbf{U}_P = \mathbf{u}_{\mathrm{proxy}}$, where $\mathbf{u}_{\mathrm{proxy}}$ is taken to be one of $\mathbf{0}$, $\mathbf{u}_{160}$, $\mathbf{u}_{\sigma_P \mathrm{peak}}$, or $\mathbf{u}_{\sigma_H \mathrm{peak}}$. These are respectively the zero vector, the neutral wind at 160-km altitude, the neutral wind at the altitude where the Pedersen conductivity profile peaks, and the neutral wind at the altitude where the Hall conductivity profile peaks. Each distribution is presented as a vertical box plot, where each box indicates (from top to bottom) the upper quartile $Q3$, the median, and lower quartile $Q1$. The horizontal lines above and below are respectively given by $Q3 + 1.5\mathrm{IQR}$ and $Q1 - 1.5\mathrm{IQR}$, where $\mathrm{IQR} = Q3 - Q1$ is the interquartile range. In analogy with Figure 3a, Figure 3b shows the error associated with assuming $\mathbf{U}_H = \mathbf{u}_{\mathrm{proxy}}$.

Figure 3a demonstrates that for the 15 neutral wind profiles examined in this study, assuming $\mathbf{U}_P = \mathbf{u}_{\sigma_P \mathrm{peak}}$ statistically incurs less error than assuming $\mathbf{U}_P = \mathbf{0}$, $\mathbf{U}_P = \mathbf{u}_{160}$, or $\mathbf{U}_P = \mathbf{u}_{\sigma_H \mathrm{peak}}$. For $\mathbf{U}_H$, Figure 3b shows that assuming $\mathbf{U}_H = \mathbf{0}$ incurs the least median error of any proxy, although the overall range of errors is smallest for $\mathbf{U}_H = \mathbf{u}_{\sigma_H \mathrm{peak}}$.

Lu et al. (1995) found via simulation that the "effective neutral wind pattern" $\mathbf{U}_P$ is equivalent to the neutral wind pattern at 160-km altitude. This rule of thumb has been employed by Baker et al. (2004) and Billett et al. (2018). Our experimental test

https://doi.org/10.5194/egusphere-2026-940
Preprint. Discussion started: 13 March 2026

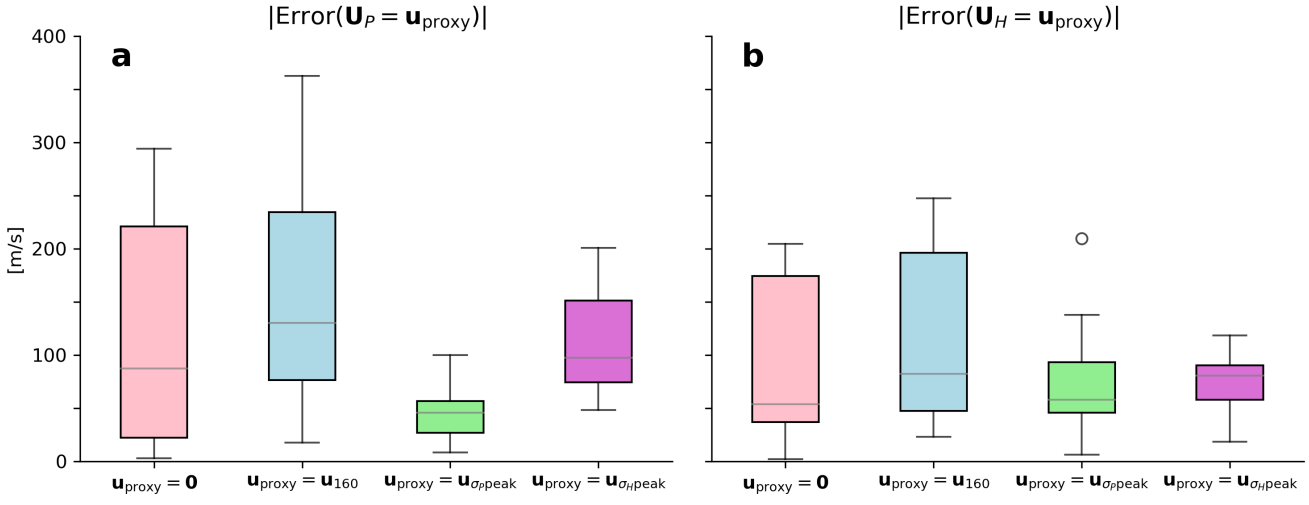

Figure 3. (a) For 15 neutral wind profiles, statistics of the magnitude of the Pedersen-weighted neutral wind ($\mathbf{U}_P$, pink), the magnitude of the differences between $\mathbf{U}_P$ and the neutral wind at 160-km altitude ($\mathbf{u}_{160}$, blue), the magnitude of the difference between $\mathbf{U}_P$ and the neutral wind at the height at which the Pedersen conductance maximizes ($\mathbf{u}_{\sigma_P\text{peak}}$, green), and the magnitude of the difference between $\mathbf{U}_P$ and the neutral wind at the height at which the Hall conductance maximizes ($\mathbf{u}_{\sigma_H\text{peak}}$, violet). The first and second represent the error associated with assuming $\mathbf{U}_P = 0$ m/s and $\mathbf{U}_P = \mathbf{u}_{160}$; the latter two represent the error associated with assuming $\mathbf{U}_P$ is one of the two proxies. The horizontal lines above and below each box plot are respectively given by $Q3 + 1.5\text{IQR}$ and $Q1 - 1.5\text{IQR}$ (see main text). (b) Same as panel a, but for the Hall-weighted neutral wind $\mathbf{U}_H$. The point of this figure is to answer Question 2 posed at the beginning of Section 3 by assessing whether any proxy for the Hall- and Pedersen-weighted neutral winds statistically incurs less error than simply assuming that they are zero.

(Figure 3a) seems to refute this proposed rule of thumb, revealing that it yields a larger error than the more naïve assumption that $\mathbf{u} = \mathbf{0}$ for the majority of the 15 neutral wind profiles examined in this study.

3.4 Underestimation of wind contribution to Joule heating

To address Question 3 posed at the beginning of this Section, we compare the neutral wind term $\int \sigma_P |\mathbf{u} \times \mathbf{B}|^2 dh$ calculated by integrating the altitude profile of the product $\sigma_P\,\mathbf{u}$ with the term $\Sigma_P |\mathbf{U}_P \times \mathbf{B}|^2$ that is calculated from height-integrated quantities.

We calculate $\int \sigma_P |\mathbf{u} \times \mathbf{B}|^2 dh$ for all 15 rocket launches using the wind profile $\mathbf{u}$ measured by each rocket and the corresponding Pedersen conductivity altitude profile σ_P derived from PFISR measurements, as described in Section 3.1 and Appendix C. We then calculate for each rocket launch the lower-bound approximation of this integral, $\Sigma_P |\mathbf{U}_P \times \mathbf{B}|^2$, using each value of $\mathbf{U}_P$ presented in Section 3.2 and the height integral of the corresponding altitude profile of the Pedersen conductivity Σ_P.

Figure 4a shows that the lower-bound approximation (y axis) underestimates the true value (x axis), as expected from the analysis in Section 2. Figure 4b indicates the percent underestimation ranges from 9% to 96%, with the magnitude of

https://doi.org/10.5194/egusphere-2026-940
Preprint. Discussion started: 13 March 2026

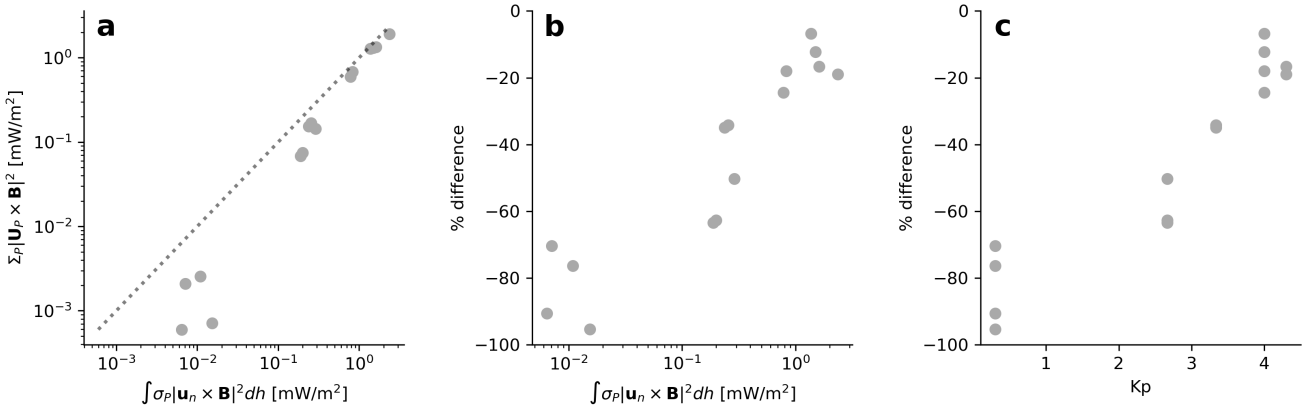

Figure 4. (a) Comparison of the difference between the integral $\int \sigma_P |\mathbf{u} \times \mathbf{B}|^2 dh$ (last term on RHS of Equation 10) calculated from altitude profiles of σ_P and $\mathbf{u}$ and the lower-bound approximation $\Sigma_P |\mathbf{U}_P \times \mathbf{B}|^2$ calculated from height-integrated quantities. (b) Percent difference between the value of the integral and the lower-bound approximation, relative to the value of the integral. (c) Percent difference as a function of Kp. The point of this figure is to answer Question 3 posed at the beginning of Section 3 as to how much the lower-bound approximation calculated from height-integrated quantities underestimates the magnitude of the true integral.

underestimation decreasing as $\int \sigma_P |\mathbf{u} \times \mathbf{B}|^2 dh$ increases. Last, Figure 4c shows that the gap between $\Sigma_P |\mathbf{U}_P \times \mathbf{B}|^2$ and $\int \sigma_p |\mathbf{u} \times \mathbf{B}|^2 dh$ tends to decrease with increasing Kp.

4 Discussion

This study aims to clear up misconceptions about how to incorporate thermospheric winds, which are sparsely sampled, and highly variable and structured in altitude, into IT data assimilation techniques that rely on 2D uniform slabs to describe IT electrodynamics.

The analysis in Section 2 shows how height integration of the ionospheric Ohm's law yields two separate neutral wind vectors (defined by Equation 9), and that height-integrated variables can only produce a lower-bound estimate of the isolated contribution of neutral winds to Joule heating (third term on the right-hand side of Equation 10). This analysis has some bearing on the "key MI coupling equation" derived from current continuity that is mentioned in the introduction,

$$\nabla \cdot \mathbf{J}_\perp = -j_\parallel, \tag{12}$$

where the integrated perpendicular current $\mathbf{J}_\perp$ is given by a height- or field line-integrated form of Ohm's law (i.e., $\mathbf{J}_\perp = \bar{\bar{\Sigma}} \cdot [\mathbf{E}_\perp + \mathbf{U} \times \mathbf{B}]$) in terms of an ionospheric conductance tensor $\bar{\bar{\Sigma}}$, the potential electric field $\mathbf{E}_\perp = -\nabla_\perp \Phi$, and an effective neutral wind $\mathbf{U}$. The development in Section 2 shows that it is strictly speaking not possible to formulate the height-integrated ionospheric Ohm's law as given by Equation 7 in terms of the conductance tensor $\bar{\bar{\Sigma}}$, because $\mathbf{F}_H$ and $\mathbf{F}_P$ are generally not identical. However, it is unclear from the results presented in Figure 3 how much the differences between $\mathbf{U}_H$ and $\mathbf{U}_P$ might

https://doi.org/10.5194/egusphere-2026-940
Preprint. Discussion started: 13 March 2026

affect the description of IT electrodynamics in models that employ some form of this equation. This topic may be the subject of a future investigation.

Regarding representation of MI coupling in global models, Equation 12 is not the state of the art: Ionosphere-thermosphere models such as the Whole Atmosphere Community Climate Model With Thermosphere and Ionosphere Extension (WACCM-X, Liu et al., 2018) and the Thermosphere-Ionosphere-Electrodynamics General Circulation Model (Qian et al., 2014) use the 2D continuity equation given in the more advanced treatment of Richmond (1995). The Richmond (1995) equation generalizes Equation 12 and does, in fact, take stock of the three-dimensional nature of the neutral wind field. Approaches similar to that of Richmond (1995) have also been presented (Maute et al., 2021; Zhu et al., 2022; Laundal et al., 2025b).

The results in Section 3 constitute the first experimental comparison of the two neutral wind vectors, showing that with increasing geomagnetic activity the difference in magnitude of these vectors increases (Figure 2b) while the vectors themselves become more aligned (Figure 2c). It is nevertheless difficult to draw general conclusions about $\mathbf{U}_H$ and $\mathbf{U}_P$ solely on the basis of the estimates shown in Figure 2a, as these estimates are representative of only one location (PFRR) for a sparsely sampled range of universal times (∼06–14 UT) and one season (January to March), as indicated in Table 1. It nevertheless seems reasonable that the range of magnitudes of $\mathbf{U}_H$ and $\mathbf{U}_P$ shown in Figure 2a is typical at high latitudes during low to moderate geomagnetic activity.

Section 3.3 addresses the commonly employed assumption in experimental studies that the winds are zero in Earth's corotating frame of reference, as well as the concept of a two-dimensional "effective neutral wind" pattern introduced by Lu et al. (1995) and employed by both Baker et al. (2004) and Billett et al. (2018). These studies take the effective neutral wind pattern to be the neutral winds at 160-km altitude, $\mathbf{u}_{160}$. Meanwhile, Figure 3 shows that the most suitable definition (i.e., the definition that incurs the least error) for the "effective neutral wind" is what we have termed the Pedersen-weighted neutral wind $\mathbf{U}_P$ given in Equation 9. The next most suitable proxy is the neutral wind at the altitude at which the Pedersen conductivity profile peaks (labeled $\mathbf{u}_{\sigma_P\text{peak}}$ in Figure 3). Figure 3 also suggests that the assumption $\mathbf{U}_H = \mathbf{U}_P = \mathbf{u}_{\sigma_P,\text{peak}}$ is likely an improvement over simply assuming $\mathbf{U}_H = \mathbf{U}_P = \mathbf{u} = 0$.

Interestingly, Figure 3 also shows that the assumption $\mathbf{u} = 0$ is statistically a better estimate for both $\mathbf{U}_H$ and $\mathbf{U}_P$ than the neutral winds at 160-km altitude, $\mathbf{u}_{160}$. While this result is likewise subject to the caveat given above regarding limited sampling, it does nevertheless indicate that one should be skeptical of "quick fixes" for the neutral wind problem, including ignoring the winds or using wind estimates from higher altitudes such as those estimated via Fabry-Perot interferometers attuned to the 630-nm line (e.g., Shiokawa et al., 2014, and references therein).

Section 3.4 provides an experimental demonstration of the analytic result that the isolated contribution of neutral winds to Joule heating ($\int \sigma_P |\mathbf{u}_n \times \mathbf{B}|^2 \, dh$, third term on the right-hand side of Equation 10) is underestimated when calculated from height-integrated quantities as $\Sigma_P |\mathbf{U}_P \times \mathbf{B}|^2$. Figure 4c shows that the contribution estimated from height-integrated quantities tends to approach the true contribution with increasing Kp.

In summary, we have here pointed out a fundamental limitation of 2D descriptions of IT electrodynamics: In a 2D representation, the governing equation (ionospheric Ohm's law) contains two neutral wind terms that are separately weighted by the altitude profiles of Hall and Pedersen conductivities. Furthermore, even when an appropriately defined neutral wind term

https://doi.org/10.5194/egusphere-2026-940
Preprint. Discussion started: 13 March 2026

is used (the Pedersen-weighted neutral wind), any estimate of height-integrated Joule heating on the basis of height-integrated and averaged quantities is mathematically guaranteed to be a lower bound of the actual height-integrated Joule heating, with some tendency for the pure neutral wind term to be less strongly underestimated with increasing Kp.

At the most basic level this study is one more voice in the chorus of recent literature calling for additional neutral wind measurements (Sarris, 2019; Heelis and Maute, 2020; Palmroth et al., 2021; Dhadly et al., 2023). However, results in Figure 3 show that estimates of height-integrated electrodynamic quantities might be improved simply by having an estimate of the neutral wind at a single altitude near the altitude at which the Pedersen conductivity peaks. This points to the utility of techniques and measurements that enable estimation of the neutral wind profiles over limited ranges of altitudes between 120 and 200 km where the Pedersen conductivity profile may peak, including Doppler spectroscopy based on emissions from atomic oxygen at 558 nm (Branning et al., 2022; Dhadly et al., 2023, and references there in) and next-generation incoherent scatter radar systems such as PFISR and the upcoming EISCAT_3D facility (Zhan and Kaeppler, 2025; Reistad et al., 2024, and references therein).

It remains to be seen how important the distinction between the Hall- and Pedersen-weighted neutral winds is for calculations of the height-integrated current density as given by Equation 7. It likewise remains to be seen whether estimates of the Hall and Pedersen conductances on the basis of estimates of the height-integrated perpendicular current and electric field, as is done by Weimer and Edwards (2021) and Hatch et al. (2024), can be improved by inclusion of limited information about the neutral winds. We suggest that it would be valuable to compare height-integrated Joule heating estimated directly from altitude profiles (Equation 10) and from height-integrated variables (Equation 4), and to carry out similar comparisons for height-integrated current density (Equation 1 versus Equation 7) and conductance ($\int \sigma_{H,P}\, dh$ versus Equation 3). Such a study would be experimentally very demanding, as it would require comprehensive information about the state of the coupled ionosphere-thermosphere system.

Code and data availability. For this study, the NRLMSIS®2.0, IRI 2016, and IGRF-13 models were respectively queried via the `nrlmsis2.0` (Hirsch, 2020), `iri2016` (Hirsch, 2018), and `ppigrf` (Laundal, 2023) Python packages. Scripts and data used to make the plots shown in this study are available at Zenodo (Hatch and Mesquita, 2024).

Appendix A: Relationship between assumed E-field height independence and scale size of variations

Here we briefly show how one effectually assumes a limit on the scale size of variations of $\mathbf{E}_\perp$ across field lines by assuming $\mathbf{E}_\perp$ does not vary with altitude.

Suppose magnetic field lines are locally tilted by an angle θ relative to the vertical direction (i.e., inclination $I = 90° - \theta$), and that we have a coordinate system $x'yz'$ that is such that z' is parallel to field lines locally and x' and y are perpendicular. This coordinate system is tilted relative to a local xyz coordinate system, with the x direction of the latter determined by ensuring that the field lines are contained within the xz plane and the z direction upward. The transformations from xyz to

https://doi.org/10.5194/egusphere-2026-940
Preprint. Discussion started: 13 March 2026

$x'yz'$ coordinates are then

$x' = x\cos\theta - z\sin\theta;$

$z' = x\sin\theta + z\cos\theta.$

The perpendicular electric field $\mathbf{E}_\perp(x', y) = \mathbf{E}_\perp(x\cos\theta - z\sin\theta, y) = E_{\perp,x'}\hat{\mathbf{x}}' + E_{\perp,y}\hat{\mathbf{y}}$.

We now examine the integral over height of the first term on the right-hand side of Equation 1,

$$\int_{z_1}^{z_2} \sigma_P(z)\mathbf{E}_\perp(x\cos\theta - z\sin\theta, y), dz, \tag{A1}$$

where for simplicity we take $\mathbf{u} = 0$. Moving $\mathbf{E}_\perp$ outside the integral requires that $\mathbf{E}_\perp$ be approximately invariant between z_1 and z_2, or equivalently (via the dependence of $\mathbf{E}_\perp$ on x') over a horizontal distance $d = (z_2 - z_1)\tan\theta$. For example, if the local field inclination $I = 70°$ and the effective vertical extent of the ionosphere $\Delta_z = z_2 - z_1 = 50$ km, assuming $\mathbf{E}_\perp$ does not vary with altitude is equivalent to assuming that it does not vary over a distance $d \approx 18$ km, or about 0.2°. The situation is more drastic in the Southern Hemisphere, where if the inclination $I = 50°$ the distance is ∼30 km, or 0.3°.

Thus one effectually assumes a limit on the scale size of variations of $\mathbf{E}_\perp$ across field lines by assuming $\mathbf{E}_\perp$ does not vary with altitude. An example of where this could be taken into account is given in the text immediately following Equation 9 in Aikio et al. (2012).

Appendix B: Cauchy-Bunyakovsky-Schwarz proof

Let $L^2_w(X, \mu)$ be a weighted L^2 space over X with measure μ. The corresponding inner product for functions f and g is

$$\langle f, g\rangle = \int_X f(t)\overline{g(t)}w(t)dt, \tag{B1}$$

with $w(t) > 0$ for all t. The inner product (B1) obeys the Cauchy-Bunyakovsky-Schwarz inequality

$|\langle f, g\rangle|^2 \le \langle f, f\rangle\langle g, g\rangle.$

Taking $f = 1$, $g = u_i$ (the i^{th} component of the neutral wind $\mathbf{u}$), and $\mu = \sigma_P$, we have

$$\left|\int \sigma_P u_i dh\right|^2 = \Sigma_P^2 U_{P,i}^2 \le \Sigma_P \int \sigma_P u_i^2 dh,$$

or rearranging,

$$\int \sigma_P u_i^2 dh \ge \Sigma_P U_{P,i}^2.$$

https://doi.org/10.5194/egusphere-2026-940
Preprint. Discussion started: 13 March 2026

Summing this inequality for each component of $\mathbf{u}$ we find

$$\int \sigma_P |\mathbf{u}|^2 dh \geq \Sigma_P |\mathbf{U}_P|^2. \tag{B2}$$

If in addition the magnetic field $\mathbf{B}$ is approximately constant between altitudes of ∼80–200 km, then multiplying both sides of Inequality B2 by $|\mathbf{B}\sin\theta|^2$ and applying the geometric definition of the cross product ($|\mathbf{u}||\mathbf{B}|\sin\theta = \mathbf{u}\times\mathbf{B}$) we have

$$\int \sigma_P |\mathbf{u}\times\mathbf{B}|^2 dh \geq \Sigma_P |\mathbf{U}_P\times\mathbf{B}|^2. \tag{B3}$$

Appendix C: Calculation of conductivity profiles

Hall and Pedersen conductivity profiles σ_H and σ_P are derived following Ieda (2020), with

$$(\sigma_H, \sigma_P) = (\sigma_{H,e} - \sigma_{H,i}, \sigma_{P,e} + \sigma_{P,i})\,. \tag{C1}$$

Subscripts e and i refer to the contributions from electrons and ions. For each conductivity the ion contribution is a sum over ion species:

$$\sigma_{\{H,P\},i} = \sum_{l=\mathrm{NO}^+,\mathrm{O}_2^+,\mathrm{O}^+} \sigma_{\{H,P\},l}. \tag{C2}$$

The contribution from each charged particle species j (NO^+, O_2^+, O^+, and e^-) is given by

$$(\sigma_{H,j}, \sigma_{P,j}) = \frac{en_j}{B}\left(\frac{k_j^2}{1+k_j^2}, \frac{k_j}{1+k_j^2}\right), \tag{C3}$$

with $k_j = \Omega_j/\nu_{jn}$, and Ω_j and ν_{jn} respectively the gyrofrequency and collision frequency for momentum transfer between charged particle species j and neutrals.

Expressions for ν_{jn} are given in Appendix A of Ieda (2020) for the three ion species just mentioned and neutral species N_2, O_2, and O. These expressions take stock of non-resonant collisions between parental pairs such as O_2^+ and O_2 that are neglected by, for example, Schunk and Nagy (2009), but are nevertheless an essential part of the description of ion-neutral collisions for ion and neutral temperatures below approximately 600 K.

Figure C1 illustrates the quantities involved in the calculation of conductivity for a wind profile measured during the Mesospheric Inversion Layer Stratified Turbulence (MIST) campaign on January 26, 2015. In Figure C1a densities of neutral species are given by the NRLMSIS®2.0 empirical atmospheric model (Emmert et al., 2020). In Figure C1b the electron density (labeled e^-) is measured by PFISR, and the ion species densities are given by multiplying the electron density by the fractional composition of each species as given by the International Reference Ionosphere (IRI) 2016 model (Bilitza et al., 2017). In Figure C1c the electron and ion temperatures are measured by PFISR, and the neutral temperature is given by IRI 2016.

From these density and temperature profiles we calculate collision frequencies (Figure C1d) and conductivity profiles (Figure C1e) that are ultimately used to estimate the zonal (labeled U_H and U_P) and meridional (labeled V_H and V_P) components

https://doi.org/10.5194/egusphere-2026-940
Preprint. Discussion started: 13 March 2026

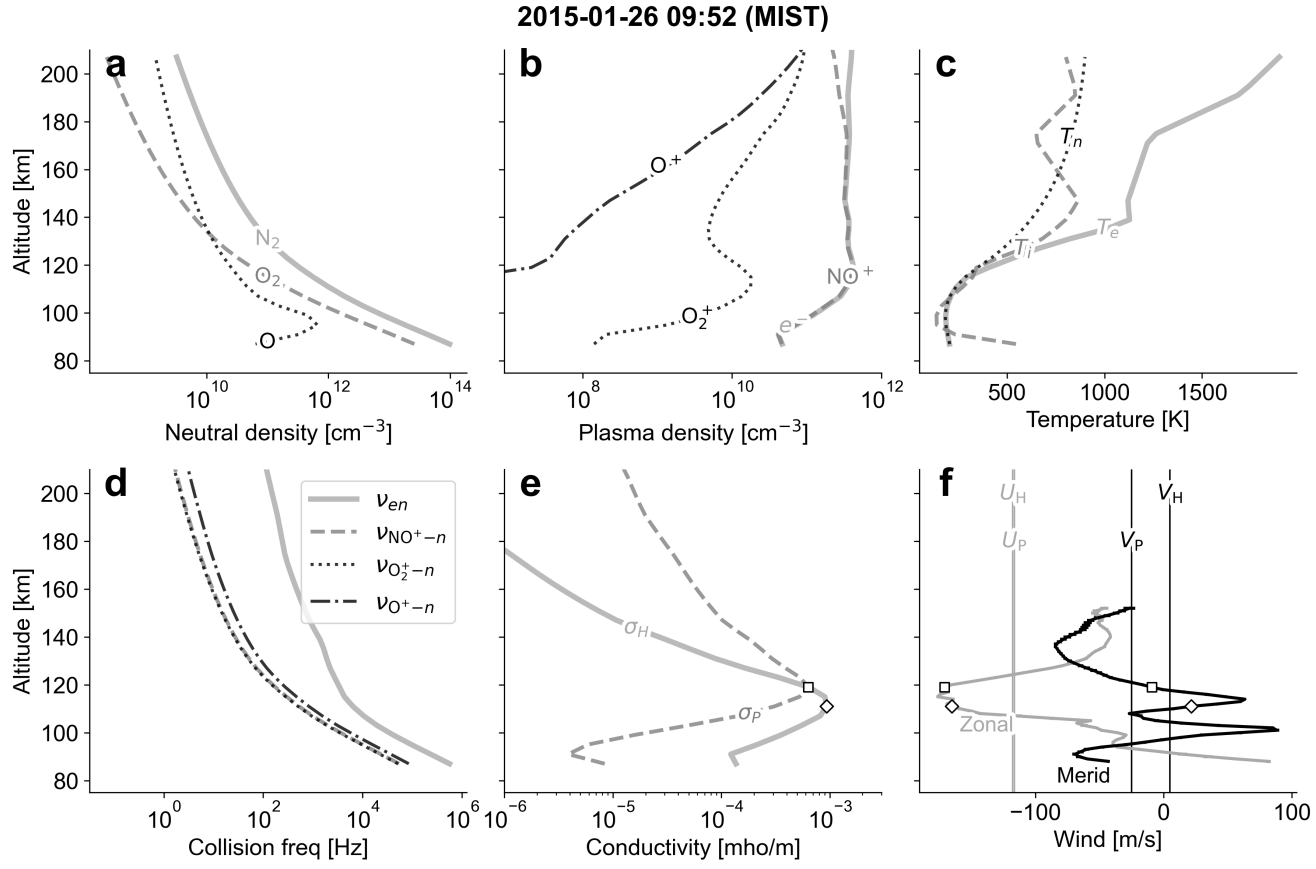

Figure C1. Illustration of altitude profiles needed for calculation of zonal and meridional components of the Hall- and Pedersen-weighted winds via Equation 9. These profiles correspond to the MIST rocket launched 2015-01-26 09:52 UT during moderate geomagnetic activity ($K_p = 4.0$; see Figure 1c1–c3). (a) Neutral density profiles from NRLMSIS®2.0 model. (b) PFISR plasma density profile (e^-) with fractional ion species densities given by IRI 2016. (c) PFISR electron and ion temperature profiles, and IRI 2016 neutral temperature profile. (d) Ion-neutral collision frequencies calculated from profiles in panels a–c. (e) Hall and Pedersen conductivity profiles (solid and dashed lines). The peaks of the Hall and Pedersen conductivity profiles are respectively indicated by a diamond and a square. (f) Neutral wind profiles. Zonal (U_H and U_P) and meridional (V_H and V_P) components of the Hall- and Pedersen-weighted neutral winds are indicated with vertical lines. Neutral wind components at peaks of the Hall and Pedersen conductivity profiles respectively also indicated by diamond and square symbols.

https://doi.org/10.5194/egusphere-2026-940
Preprint. Discussion started: 13 March 2026

of the Hall- and Pedersen-weighted neutral winds, which are indicated with vertical lines in Figure C1f. The Supplement contains figures corresponding to Figure C1 for the remaining 14 wind profiles.

Author contributions. SMH: Conceptualization, methodology, software, formal analysis, writing, investigation, visualization, funding acquisition. JKB: Validation, manuscript review and editing. HV: Conceptualization, validation, manuscript review and editing. RM: Data curation, manuscript review and editing. KML: Validation, manuscript review and editing.

Competing interests. The authors declare no competing interests.

Acknowledgements. This study is supported as part of Swarm Data, Innovation, and Science Cluster (DISC) activities, and is funded by ESA contract no. 4000109587/13/I-NB. SMH was also funded by the Research Council of Norway (RCN) under contract 344061. JKB was supported with funding from Canadian Space Agency grant 15SUSWARM. RM was supported with funding from NASA Grant with contract number 80NSSC23K0094. HV is supported by the Research Council of Finland project 354521. KML is funded by the European Union (ERC, DynaMIT, 101086985). The authors thank A. Bhatt (SRI) for helpful guidance regarding the use of PFISR data.

https://doi.org/10.5194/egusphere-2026-940
Preprint. Discussion started: 13 March 2026

References

Aikio, A. T., Cai, L., and Nygrén, T.: Statistical distribution of height-integrated energy exchange rates in the ionosphere, Journal of Geophysical Research: Space Physics, 117, https://doi.org/10.1029/2012JA018078, 2012.

Akbari, H., Pfaff, R., Clemmons, J., Freudenreich, H., Rowland, D., and Streltsov, A.: Resonant Alfvén Waves in the Lower Auroral Ionosphere: Evidence for the Nonlinear Evolution of the Ionospheric Feedback Instability, Journal of Geophysical Research: Space Physics, 127, https://doi.org/10.1029/2021JA029854, 2022.

Amm, O.: The elementary current method for calculating ionospheric current systems from multisatellite and ground magnetometer data, Journal of Geophysical Research: Space Physics, 106, 24 843–24 855, https://doi.org/10.1029/2001JA900021, 2001.

Baker, J. B. H., Zhang, Y., Greenwald, R. A., Paxton, L. J., and Morrison, D.: Height-integrated Joule and auroral particle heating in the night side high latitude thermosphere, Geophysical Research Letters, 31, https://doi.org/10.1029/2004GL019535, 2004.

Bilitza, D., Altadill, D., Truhlik, V., Shubin, V., Galkin, I., Reinisch, B., and Huang, X.: International Reference Ionosphere 2016: From ionospheric climate to real-time weather predictions, Space Weather, 15, 418–429, https://doi.org/10.1002/2016SW001593, 2017.

Billett, D. D., Grocott, A., Wild, J. A., Walach, M.-T., and Kosch, M. J.: Diurnal Variations in Global Joule Heating Morphology and Magnitude Due To Neutral Winds, Journal of Geophysical Research: Space Physics, 123, 2398– 2411, https://doi.org/10.1002/2017JA025141, 2018.

Branning, K., Conde, M., Larsen, M., and Troyer, R.: Resolving Vertical Variations of Horizontal Neutral Winds in Earth's High Latitude Space-Atmosphere Interaction Region (SAIR), Journal of Geophysical Research: Space Physics, 127, https://doi.org/10.1029/2021JA029805, 2022.

Burchill, J. K., Clemmons, J. H., Knudsen, D. J., Larsen, M., Nicolls, M. J., Pfaff, R. F., Rowland, D., and Sangalli, L.: High-latitude E region ionosphere-thermosphere coupling: A comparative study using in situ and incoherent scatter radar observations, Journal of Geophysical Research: Space Physics, 117, https://doi.org/10.1029/2011JA017175, 2012.

Chapman, S.: The electrical conductivity of the ionosphere: A review, Il Nuovo Cimento, 4, 1385–1412, https://doi.org/10.1007/BF02746310, 1956.

Cole, K.: Energy deposition in the thermosphere caused by the solar wind, Journal of Atmospheric and Terrestrial Physics, 37, 939–949, https://doi.org/10.1016/0021-9169(75)90008-2, 1975.

Dhadly, M., Sassi, F., Emmert, J., Drob, D., Conde, M., Wu, Q., Makela, J., Budzien, S., and Nicholas, A.: Neutral winds from mesosphere to thermosphere—past, present, and future outlook, Frontiers in Astronomy and Space Sciences, 9, https://doi.org/10.3389/fspas.2022.1050586, 2023.

Emmert, J. T., Drob, D. P., Picone, J. M., Siskind, D. E., Jones, M., Mlynczak, M. G., Bernath, P. F., Chu, X., Doornbos, E., Funke, B., Goncharenko, L. P., Hervig, M. E., Schwartz, M. J., Sheese, P. E., Vargas, F., Williams, B. P., and Yuan, T.: NRLMSIS 2.0: A whole-atmosphere empirical model of temperature and neutral species densities, Earth and Space Science, https://doi.org/10.1029/2020EA001321, 2020.

Farley, D. T.: A theory of electrostatic fields in a horizontally stratified ionosphere subject to a vertical magnetic field, Journal of Geophysical Research, 64, 1225–1233, https://doi.org/10.1029/JZ064i009p01225, 1959.

Green, D. L., Waters, C. L., Korth, H., Anderson, B. J., Ridley, A. J., and Barnes, R. J.: Technique: Large-scale ionospheric conductance estimated from combined satellite and ground-based electromagnetic data, Journal of Geophysical Research: Space Physics, 112, https://doi.org/10.1029/2006JA012069, 2007.

https://doi.org/10.5194/egusphere-2026-940
Preprint. Discussion started: 13 March 2026

Hatch, S. M. and Mesquita, R. L. A.: Resource for Hatch et al (2024), "What is the neutral wind in height-integrated electrodynamics?", https://doi.org/10.5281/zenodo.11091983, 2024.

Hatch, S. M., Vanhamäki, H., Laundal, K. M., Reistad, J. P., Burchill, J. K., Lomidze, L., Knudsen, D. J., Madelaire, M., and Tesfaw, H.: Does high-latitude ionospheric electrodynamics exhibit hemispheric mirror symmetry?, Annales Geophysicae, 42, 229–253, https://doi.org/10.5194/angeo-42-229-2024, 2024.

Heelis, R. and Maute, A.: Challenges to Understanding the Earth's Ionosphere and Thermosphere, Journal of Geophysical Research: Space Physics, https://doi.org/10.1029/2019JA027497, 2020.

Heppner, J. P. and Miller, M. L.: Thermospheric winds at high latitudes from chemical release observations, Journal of Geophysical Research: Space Physics, 87, 1633–1647, https://doi.org/10.1029/JA087iA03p01633, 1982.

Hirsch, M.: iri2016, https://doi.org/10.5281/zenodo.240895, https://doi.org/10.5281/zenodo.240895, 2018.

Hirsch, M.: nrlmsis2.0, https://github.com/space-physics/nrlmsis2.0, 2020.

Huber, P. J.: Robust Regression: Asymptotics, Conjectures and Monte Carlo, The Annals of Statistics, 1, 799–821, https://doi.org/10.1214/aos/1176342503, 1973.

Ieda, A.: Ion-Neutral Collision Frequencies for Calculating Ionospheric Conductivity, Journal of Geophysical Research: Space Physics, 125, https://doi.org/10.1029/2019JA027128, 2020.

Larsen, M. F.: Winds and shears in the mesosphere and lower thermosphere: Results from four decades of chemical release wind measurements, Journal of Geophysical Research: Space Physics, 107, SIA 28–1–SIA 28–14, https://doi.org/10.1029/2001JA000218, 2002.

Larsen, M. F., Pfaff, R. F., Mesquita, R., and Kaeppler, S. R.: Gradient Winds and Neutral Flow Dawn-Dusk Asymmetry in the Auroral Oval During Geomagnetically Disturbed Conditions, Journal of Geophysical Research: Space Physics, 127, https://doi.org/10.1029/2021JA029936, 2022.

Laundal, K. M.: Pure Python International Geomagnetic Reference Field (ppigrf), https://doi.org/10.5281/zenodo.5962660, 2023.

Laundal, K. M., Reistad, J. P., Hatch, S. M., Madelaire, M., Walker, S., Hovland, A. Ø., Ohma, A., Merkin, V. G., and Sorathia, K. A.: Local Mapping of Polar Ionospheric Electrodynamics, Journal of Geophysical Research: Space Physics, 127, https://doi.org/10.1029/2022JA030356, 2022.

Laundal, K. M., Marchaudon, A., Maute, A., Hatch, S. M., Enengl, F., Matsuo, T., Decotte, M., Madelaire, M., Merkin, V. G., Sciola, A., Haberle, V., and Skeidsvoll, A. S.: Next-Generation Data Assimilation Methods for Polar Ionospheric Electrodynamics, Surveys in Geophysics, https://doi.org/10.1007/s10712-025-09918-3, 2025a.

Laundal, K. M., Skeidsvoll, A. S., Braileanu, B. P., Hatch, S. M., Olsen, N., and Vanhamäki, H.: Global inductive magnetosphere-ionosphere-thermosphere coupling, Annales Geophysicae, 43, 803–833, https://doi.org/10.5194/angeo-43-803-2025, 2025b.

Liu, H., Bardeen, C. G., Foster, B. T., Lauritzen, P., Liu, J., Lu, G., Marsh, D. R., Maute, A., McInerney, J. M., Pedatella, N. M., Qian, L., Richmond, A. D., Roble, R. G., Solomon, S. C., Vitt, F. M., and Wang, W.: Development and Validation of the Whole Atmosphere Community Climate Model With Thermosphere and Ionosphere Extension (WACCM-X 2.0), Journal of Advances in Modeling Earth Systems, 10, 381–402, https://doi.org/10.1002/2017MS001232, 2018.

Lu, G., Richmond, A. D., Emery, B. A., and Roble, R. G.: Magnetosphere-ionosphere-thermosphere coupling: Effect of neutral winds on energy transfer and field-aligned current, Journal of Geophysical Research: Space Physics, 100, 19 643–19 659, https://doi.org/10.1029/95JA00766, 1995.

https://doi.org/10.5194/egusphere-2026-940
Preprint. Discussion started: 13 March 2026

Mannucci, A. J., McGranaghan, R., Meng, X., and Verkhoglyadova, O. P.: An Analysis of Magnetosphere-Ionosphere Coupling That Is Independent of Inertial Reference Frame, Journal of Geophysical Research: Space Physics, 127, https://doi.org/10.1029/2021JA030009, 2022.

Matsuo, T.: Recent Progress on Inverse and Data Assimilation Procedure for High-Latitude Ionospheric Electrodynamics, pp. 219–232, Springer International Publishing, https://doi.org/10.1007/978-3-030-26732-2_10, 2020.

Maute, A., Richmond, A. D., Lu, G., Knipp, D. J., Shi, Y., and Anderson, B.: Magnetosphere-Ionosphere Coupling via Prescribed Field-Aligned Current Simulated by the TIEGCM, Journal of Geophysical Research: Space Physics, 126, https://doi.org/10.1029/2020JA028665, 2021.

Merkin, V. G. and Lyon, J. G.: Effects of the low-latitude ionospheric boundary condition on the global magnetosphere, Journal of Geophysical Research: Space Physics, 115, https://doi.org/10.1029/2010JA015461, 2010.

Mesquita, R. L. A.: An Observational Investigation of Mid-Latitude Thermospheric Temperatures and High-Latitude E-Region Neutral Wind Structures, Dissertation, Clemson University, https://tigerprints.clemson.edu/all_dissertations/2802/, 2021.

Mesquita, R. L. A., Larsen, M. F., Azeem, I., Stevens, M. H., Williams, B. P., Collins, R. L., and Li, J.: In Situ Observations of Neutral Shear Instability in the Statically Stable High-Latitude Mesosphere and Lower Thermosphere During Quiet Geomagnetic Conditions, Journal of Geophysical Research: Space Physics, 125, https://doi.org/10.1029/2020JA027972, 2020.

Mukhopadhyay, A., Jia, X., Welling, D. T., and Liemohn, M. W.: Global Magnetohydrodynamic Simulations: Performance Quantification of Magnetopause Distances and Convection Potential Predictions, Frontiers in Astronomy and Space Sciences, 8, https://doi.org/10.3389/fspas.2021.637197, 2021.

Palmroth, M., Grandin, M., Sarris, T., Doornbos, E., Tourgaidis, S., Aikio, A., Buchert, S., Clilverd, M. A., Dandouras, I., Heelis, R., Hoffmann, A., Ivchenko, N., Kervalishvili, G., Knudsen, D. J., Kotova, A., Liu, H.-L., Malaspina, D. M., March, G., Marchaudon, A., Marghitu, O., Matsuo, T., Miloch, W. J., Moretto-Jørgensen, T., Mpaloukidis, D., Olsen, N., Papadakis, K., Pfaff, R., Pirnaris, P., Siemes, C., Stolle, C., Suni, J., van den IJssel, J., Verronen, P. T., Visser, P., and Yamauchi, M.: Lower-thermosphere–ionosphere (LTI) quantities: current status of measuring techniques and models, Annales Geophysicae, 39, 189–237, https://doi.org/10.5194/angeo-39-189-2021, 2021.

Parker, E. N.: Conversations on Electric and Magnetic Fields in the Cosmos, Princeton University Press, ISBN 9781400847433, https://doi.org/10.2307/j.ctt2111gdt, 2007.

Qian, L., Burns, A. G., Emery, B. A., Foster, B., Lu, G., Maute, A., Richmond, A. D., Roble, R. G., Solomon, S. C., and Wang, W.: The NCAR TIE-GCM, pp. 73–83, John Wiley & Sons, Ltd, ISBN 9781118704417, https://doi.org/10.1002/9781118704417.ch7, 2014.

Reistad, J. P., Hatch, S. M., Laundal, K. M., Oksavik, K., Zettergren, M. D., Vanhamäki, H., and Virtanen, I. I.: Volumetric reconstruction of ionospheric electric currents from tri-static incoherent scatter radar measurements, ESS Open Archive, 2024.

Richmond, A. D.: Ionospheric Electrodynamics Using Magnetic Apex Coordinates, Journal of geomagnetism and geoelectricity, 47, 191–212, https://doi.org/10.5636/jgg.47.191, 1995.

Richmond, A. D. and Kamide, Y.: Mapping electrodynamic features of the high-latitude ionosphere from localized observations - Technique, Journal of Geophysical Research, 93, 5741–5759, https://doi.org/10.1029/JA093iA06p05741, 1988.

Sangalli, L., Knudsen, D. J., Larsen, M. F., Zhan, T., Pfaff, R. F., and Rowland, D.: Rocket-based measurements of ion velocity, neutral wind, and electric field in the collisional transition region of the auroral ionosphere, Journal of Geophysical Research: Space Physics, 114, https://doi.org/10.1029/2008JA013757, 2009.

https://doi.org/10.5194/egusphere-2026-940
Preprint. Discussion started: 13 March 2026

Sarris, T. E.: Understanding the ionosphere thermosphere response to solar and magnetospheric drivers: status, challenges and open issues, Philosophical Transactions of the Royal Society A: Mathematical, Physical and Engineering Sciences, 377, 20180 101, https://doi.org/10.1098/rsta.2018.0101, 2019.

Schunk, R. and Nagy, A.: Ionospheres, Cambridge University Press, Cambridge, second edn., ISBN 9780511635342, https://doi.org/10.1017/CBO9780511635342, 2009.

Scott, T.: Analysis of the Neutral Wind Profiles from the HEX II Experiment, 2009.

Shiokawa, K., Kadota, T., Otsuka, Y., Ogawa, T., Nakamura, T., and Fukao, S.: A two-channel Fabry-Perot interferometer with thermoelectric-cooled CCD detectors for neutral wind measurement in the upper atmosphere, Earth, Planets and Space, 55, 271–275, https://doi.org/10.1186/BF03351759, 2014.

Thayer, J. P.: Height-resolved Joule heating rates in the high-latitude E region and the influence of neutral winds, Journal of Geophysical Research: Space Physics, 103, 471–487, https://doi.org/10.1029/97JA02536, 1998.

Vasyliunas, V. M.: The physical basis of ionospheric electrodynamics, Ann. Geophys., 30, https://doi.org/10.5194/angeo-30-357-2012, 2012.

Virtanen, P., Gommers, R., Oliphant, T. E., Haberland, M., Reddy, T., Cournapeau, D., Burovski, E., Peterson, P., Weckesser, W., Bright, J., van der Walt, S. J., Brett, M., Wilson, J., Millman, K. J., Mayorov, N., Nelson, A. R. J., Jones, E., Kern, R., Larson, E., Carey, C. J., Polat, İ., Feng, Y., Moore, E. W., VanderPlas, J., Laxalde, D., Perktold, J., Cimrman, R., Henriksen, I., Quintero, E. A., Harris, C. R., Archibald, A. M., Ribeiro, A. H., Pedregosa, F., van Mulbregt, P., and SciPy 1.0 Contributors: SciPy 1.0: Fundamental Algorithms for Scientific Computing in Python, Nature Methods, 17, 261–272, https://doi.org/10.1038/s41592-019-0686-2, 2020.

Weimer, D. and Edwards, T.: Testing the electrodynamic method to derive height-integrated ionospheric conductances, Annales Geophysicae, 39, 31–51, https://doi.org/10.5194/angeo-39-31-2021, 2021.

Zhan, W. and Kaeppler, S. R.: Seasonal and Geomagnetic Activity Dependence of Auroral E-Region Neutral Winds at Poker Flat, Journal of Geophysical Research: Space Physics, 130, https://doi.org/10.1029/2024JA033074, 2025.

Zhu, Q., Lu, G., Maute, A., Deng, Y., and Anderson, B.: Assessment of Using Field-Aligned Currents to Drive the Global Ionosphere Thermosphere Model: A Case Study for the 2013 St Patrick's Day Geomagnetic Storm, Space Weather, 20, https://doi.org/10.1029/2022SW003170, 2022.